Compared microstructure and properties of an AlZnMgCu alloy processed by high pressure sliding and high-pressure torsion

Amandine Duchaussoy, Xavier Sauvage, Alexis Deschamps, Frederic de Geuser, Gilles Renou, Zenji Horita

To cite this version:

Amandine Duchaussoy, Xavier Sauvage, Alexis Deschamps, Frederic de Geuser, Gilles Renou, et al.. Compared microstructure and properties of an AlZnMgCu alloy processed by high pressure sliding and high-pressure torsion. Journal of Alloys and Compounds, 2023, 942, pp.169060. 10.1016/j.jallcom.2023.169060 . hal-03969277

HAL Id: hal-03969277
https://hal.science/hal-03969277v1

Submitted on 2 Feb 2023

Compared microstructure and properties of an AlZnMgCu alloy processed by high pressure sliding and high-pressure torsion

Amandine Duchaussoy, Xavier Sauvage, Alexis Deschamps, Frederic De Geuser, Gilles Renou, Zenji Horita

PII: S0925-8388(23)00363-8

DOI: https://doi.org/10.1016/j.jallcom.2023.169060

Reference: JALCOM169060

To appear in: *Journal of Alloys and Compounds*

Received date: 17 November 2022
Revised date: 25 January 2023
Accepted date: 26 January 2023

Please cite this article as: Amandine Duchaussoy, Xavier Sauvage, Alexis Deschamps, Frederic De Geuser, Gilles Renou and Zenji Horita, Compared microstructure and properties of an AlZnMgCu alloy processed by high pressure sliding and high-pressure torsion, *Journal of Alloys and Compounds,* (2022) doi:https://doi.org/10.1016/j.jallcom.2023.169060

Compared microstructure and properties of an AlZnMgCu alloy processed by high pressure sliding and high-pressure torsion

Amandine Duchaussoy[1,2,*], Xavier Sauvage[1], Alexis Deschamps[3], Frederic De Geuser[3], Gilles Renou[3], Zenji Horita[4,5]

[1] *Normandie Univ, UNIROUEN, INSA Rouen, CNRS, Groupe de Physique des Matériaux, 76000 Rouen, France*

[2] *Institute of Mechanics, Materials and Civil Engineering (iMMC-IMAP), Université catholique de Louvain, 1348, Louvain-La-Neuve, Belgium*

[3] *Univ. Grenoble Alpes, CNRS, Grenoble INP, SIMaP, F-38000 Grenoble, France*

[4] *WPI, International Institute for Carbon-Neutral Energy Research (I2CNER), Kyushu University, Fukuoka 819-0395, Japan*

[5] *Department of Materials Science and Engineering, Faculty of Engineering, Kyushu University, Fukuoka 819-0395, Japan*

**Correspondence: duchaussoy.amandine@laposte.net*

Abstract:

Achieving high yield strength via submicrometer grain size and nanoscaled precipitation has been reached in 7### aluminum alloys thanks to severe plastic deformation (SPD) by High Pressure Torsion (HPT) process. Unfortunately, this technique has inherently strong limitations since only small parts can be processed and the plastic strain is not homogeneous. These limitations prevent large scale production of Ultra Fine Grain (UFG) materials for potential applications. A recent severe plastic deformation process, High Pressure Sliding (HPS) developed by Fujioka and Horita, allows to homogeneously deform large scale sheets by shear at higher speed. In this work, the competition between precipitation, grain growth and recrystallization during heat treatments after SPD was studied in depth for an AlZnMgCu alloys deformed by HPS with two deformation levels ($\gamma \approx 15$ and $\gamma \approx 20$) in order to investigate if the high mechanical properties obtained by HPT can be reached by HPS. Microstructures analyses after deformation and ageing were carried out by transmission electron microscopy and *in situ* small angle X ray scattering and then related to the mechanical behavior evaluated by tensile tests. Experimental data show very similar microstructures after HPS and HPT, with a good thermal stability thanks to the competition between precipitation, recrystallization and recovery. The obtained microstructural features lead to exceptional yield strength (>800MPa) as compared to the classical aluminum alloys. This study is therefore very promising towards the aim of obtaining very high yield strength aluminum alloys suitable for applications.

1. Introduction

Over the last two decades, designing ultrafine grain (UFG) materials has been the object of large research efforts. The specific physical and mechanical properties of UFG materials are of great potential interest for a variety of structural and functional applications requiring e.g. fatigue properties [1,2], superplastic properties [3] or high mechanical strength [4–6].

UFG structures can be obtained using two approaches: i) “bottom up” techniques to build directly UFG structures with processes such as inert gas condensation [7], electrodeposition [8], and chemical and physical deposition [9] ; (ii) “top down” approach by reducing the microstructure scale of bulk materials. This second approach is classically achieved using severe plastic deformation (SPD) methods where very large strains are applied under high hydrostatic pressure, leading to strong grain refinement in metallic alloys[10]. The most popular techniques are accumulative roll bounding (ARB) [11], equal channel angular pressing (ECAP) [12,13] and high pressure torsion (HPT) [14,15] .

Metallic alloys processed by SPD usually exhibit a significant increase of the mechanical strength that results from the grain size reduction [4–6]. Further increase can be achieved when it is combined with other strengthening mechanisms, and particularly with precipitation [5,16–18]. However, such combination is difficult to obtain because of two competing mechanisms during post deformation precipitation treatment, namely spatial redistribution of solutes and grain growth. The spatial redistribution of solutes gives rise to segregation on crystalline defects and/or decomposition of the solid solution [17,19–25]. These phenomena generally lead to heterogeneous precipitation along dislocations or grain boundaries during annealing, with a reduced precipitate number density (as compared to bulk materials) and thus a relatively modest strengthening. Besides, the high density of crystalline defects in SPD materials lead to a much higher atomic mobility and thus typically to a much faster precipitation kinetics as compared to coarse grained alloys. Additionally, the temperature needed for precipitation can widely affect the grain structure [26]. Despite these issues, successful combinations of ultrafine grain size and intense precipitation have been achieved, with mechanical strength records in metallic alloys [5,16–18].

Usually, highest yield strengths are obtained for highest levels of deformation, which can be only obtained by HPT. For example, in AlZnMgCu alloys, yield strengths between 450 and 700 MPa were reported for samples deformed using the ECAP process (true strain between 1 and 6) [17,27–32] while it is typically in a range of 650 to 990 MPa with the HPT process (true strain larger than 100) [5,33–35]. Unfortunately, the HPT process has inherently strong limitations: i) only very small discs can be deformed (typically 10 to 30 mm in diameter)[15,36], ii) the plastic strain is not homogenous, minimal in the center and maximal at the periphery [36,37]. These limitations prevent large scale production of UFG materials for potential applications. To overcome these disadvantages, Fujioka and Horita [38] have proposed a new process in 2009, namely high pressure sliding (HPS),which allows to homogeneously deform large scale sheets by shear at higher speed (a comparison between HPS and HPT is given in Table 1 : Parameters used for HPT and HPS processing). A significantly lower level of deformation can be applied by HPS with a plastic strain between 5 and 30 while it may be larger than 1000 for HPT. However, the

HPS process can be developed as a continuous process, making it quite promising for large scale production and potential industrialization [36,39].

In our previous work [5] we showed that deforming an AlZnMgCu alloy up to a true strain of 200 using HPT resulted in a grain size below 500 nm with high fraction of high angle grain boundaries (HAGBs) and a high dislocation density. Furthermore, using appropriate low temperature annealing treatments it was possible to combine this UFG structure with intra and intergranular precipitation to achieve exceptionally high mechanical strength.

The aim of the present study was to evaluate the potential of HPS to reach comparable microstructures as those obtained in our previous work by HPT [5]. The objective was first to quantify the microstructural differences between the alloys deformed by HPT and HPS, both in the as deformed state and after precipitation heat treatments, and then to establish relationships with the mechanical properties. Particularly, this study aims at determining if the lower deformation obtained by HPS as compared to HPT has a significant impact on grain size, grain boundary structure, precipitation mechanisms and thermal stability of UFG structures.
These goals have been achieved by combining complementary experimental techniques enabling the evaluation of the microstructure at the different scales and *in situ* during the post deformation heat treatments, namely: transmission electron microscopy (TEM) both using high angular annular dark field imaging (HAADF) and automated crystal orientation mapping (ACOM), small angle X ray scattering (SAXS), and tensile tests.

2. Material and Experimental methods

In this study, AlZnMgCu alloy contains as major alloying elements 8.6% Zn, 2.5% Cu and 2.1% Mg with the other elements 0.4%Fe, 0.1% Zr and 0.04% Si (in wt%). The alloy was as homogenized cylinders of 5 cm in diameter and 10 cm height by Constellium C-TEC.

A solution treatment for 1h at 474°C followed by a quenching into cold water was applied to allow a post deformation precipitation. After this treatment, to prevent natural ageing before deformation, the sample was directly brought to an ice box.

Disc shape samples (10mm diameter, 1 mm thickness) were processed by HPT under a pressure of 6GPa with 10 turns at room temperature and a rotation speed of 1rpm. Sheets of 100*10mm^2 and 1mm thickness were processed under a pressure of 3GPa with two different sliding distances (10mm and 15mm), at room temperature with a speed of 1mm.s^{-1} using the HPS facility reported earlier [39]. In both cases temperature measurements ensured that the sample temperature did not reach more than 50°C. The deformed samples were subsequently exposed to room temperature, and this led to natural ageing of 2 weeks.

If the compression strain is neglected and the sample dimensions supposed to remain constant, then the shear strain during HPT is given by [40]:

$$\gamma = \frac{2\pi N r}{h} \qquad (1)$$

and depends on the thickness of the disc h, on the distance from the disc edge r and the revolutions number N.

This shows that the disc is deformed inhomogeneously, with more intense deformation at the edge than in the center, that is typical from the HPT process [37,41–45]. In order to allow comparison of the different results, the samples were systematically taken at 2.5mm from the edge of the HPT disc, which corresponds to a shear deformation of $\gamma \approx 200$ (after 10 revolutions).

With the same approximation than HPT, the shear strain during HPS is given by [38]:

$$\gamma = \frac{x}{h} \tag{2}$$

where x is the plunger sliding distance.

Contrary to HPT, the shear deformation applied by HPS is homogeneous in the whole sample, it is $\gamma \approx 15$ and $\gamma \approx 20$ for the 10mm and 15mm sliding distances respectively. Table 1 summarizes the parameters used for HPT and HPS processing.

	High Pressure Torsion		**High Pressure Sliding**	
Pressure P(GPa)	6		3	
Deformation rate $\dot{\varepsilon}$(s^{-1})	0.75		1.25	
Deformation	Numbers of turns	Shear strain	Sliding distance (mm)	Shear strain
	10	200	10	15
			15	20

Table 1 : Parameters used for HPT and HPS processing

Mechanical properties were evaluated thanks to tensile tests. Dog bone shaped specimens were cut from the HPT discs and the HPS sheets using an electrical spark discharge machine (EDM) with gauge dimension of 1.5 mm length, 0.7 mm width and between 0.5 to 0.7 mm thickness. For HPT sample, only 1 specimen could be cut by disc, with the gauge area positioned at 2.5mm radius. For the HPS sheets, 14 specimens could be cut by sample, and they were specially distributed to allow the evaluation of the deformation homogeneity (including different orientations to the shear direction). The tensile tests were conducted at room temperature with a constant cross head speed (initial strain rate of 3.10^{-3} s^{-1}). The samples were pulled horizontally until failure.

A schematic representation of the position of the dog bone sampling zones is shown in Figure 1.

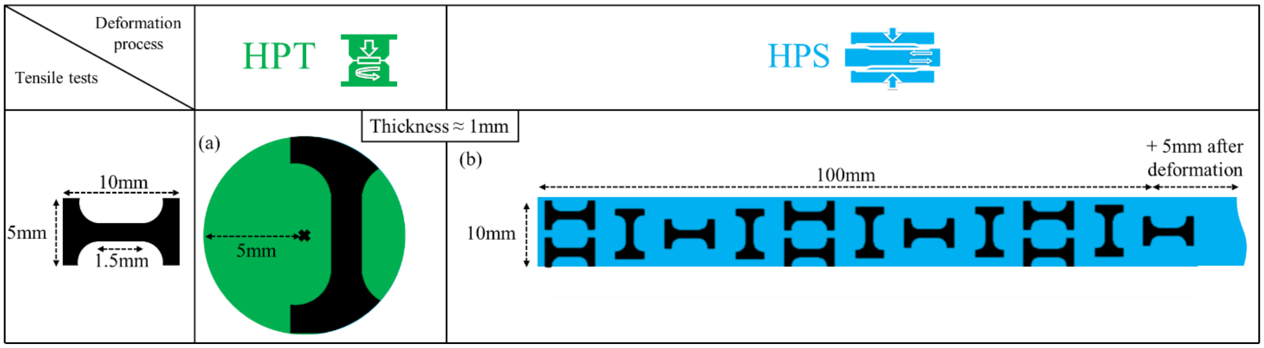

Figure 1:Schematic representation of the position of dog bone sampling on (a) HPT sample and (b) HPS sample.

Microstructure characterizations were conducted by TEM with a JEOL ARM200F microscope operated at 200 kV. STEM high angle annular dark field (HAADF) images were recorded with collection angles ranging from 80 to 180 mrad and from 20 to 80 mrad for dark field (DF) images. Both were recorded with a probe size of 0.2 nm and a convergence angle of 34 mrad. Electron transparent specimens were prepared with a twin jet electro polisher (TENUPOL 5 from Struers®) using a mixture of 30%HNO3+70% CH3OH (%vol) at − 30 °C. Final thinning was carried out by low energy ion milling conducted with a GATAN® Precision Ion Polishing System. Orientation maps and kernel average misorientation (KAM) maps were obtained with a JEOL 2100F microscope equipped with automated crystal orientation mapping (ACOM) using scanning precession electron diffraction (SPED) (angle of 1.2°) [46–48]. KAM parameter was used to study the distribution of local misorientations inside grains or sub grains (here below a misorientation angle of 10°) and to calculate the dislocation density [49]. The geometrically necessary dislocation density ρ_{GND} was estimated from the mean degree of misorientation θ obtained in KAM [49,50]:

$$\rho_{GND} = \frac{\alpha\theta}{bd} \tag{3}$$

where b is the Burgers vector (=0.286), d the acquisition step of the map and α a constant which depend on the dislocation type (=3 [50–52]).

As in our previous work [5], dislocations density were measured by KAM thanks to the TEM mapping approach and not the usually used EBSD approach studies [50–52] because of the very fine grain structures.

SAXS measurements were performed exactly as the same procedure as in our previous work [5] both for the experimental procedures and for the data processing.

3. Results

3.1. Ultrafine grain structure after severe plastic deformation

TEM orientation maps show that in as deformed alloys (Figure 2(b-d)) ultrafine grain structures with average grain sizes of 220 ± 20 nm and 210 ± 50 nm were obtained under shear strain of γ ≈

20 by HPS and γ ≈ 200 by HPT respectively. Thus, grain sizes are relatively similar despite the large shear strain difference. Since an average grain size of 520±190 nm was obtained for the sample deformed with γ ≈ 15, then it seems that γ ≈ 20 is close to the critical shear strain required to reach a saturation of grain refinement.

Grain size distributions (Figure 2(e)) show that for the lowest shear strain (γ ≈ 15), there is a small proportion of grains below 500 nm but still a significant number of larger grains with a size of about 1 µm. At γ ≈ 20, all grains are below 600 nm in size. Last, for the HPT deformed sample (γ ≈ 200) the distribution is relatively similar to that after γ ≈ 20 with few more grains in a range 20 and 120 nm.

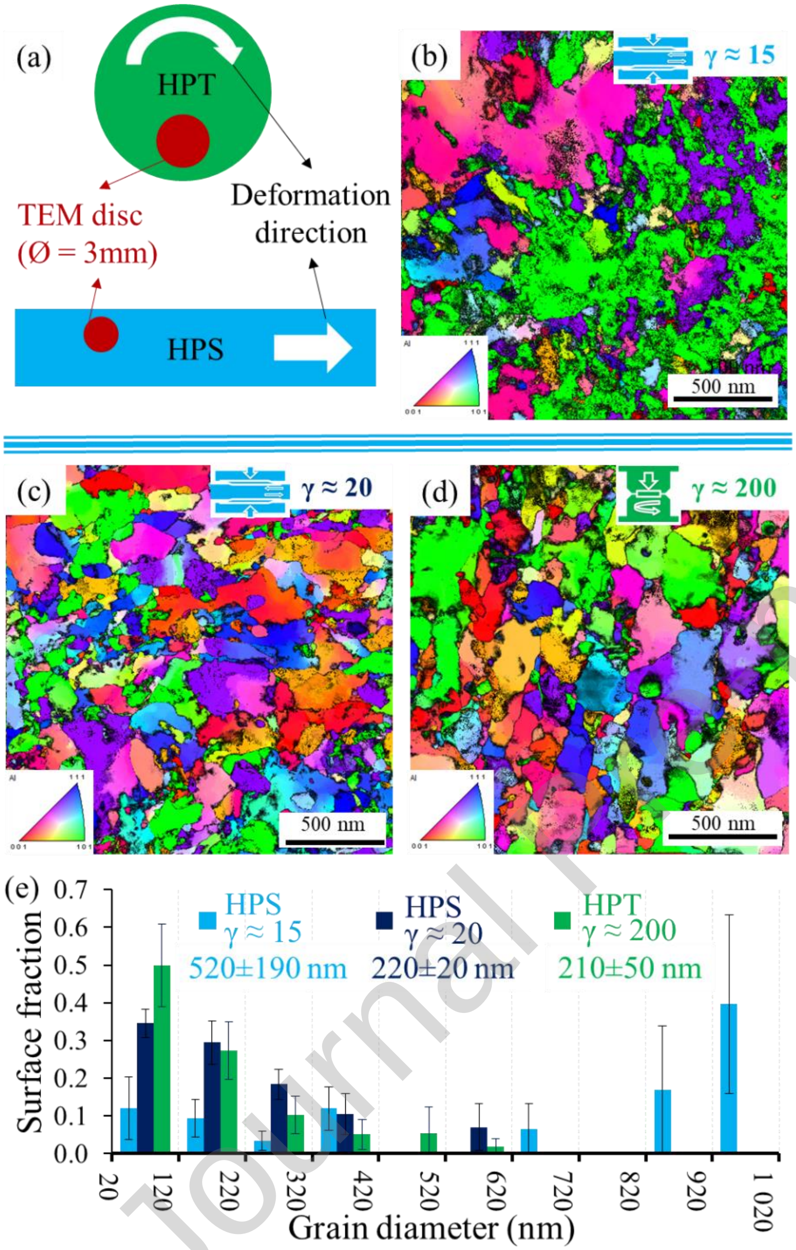

Figure 2: Schematic representation of TEM sample location for HPT and HPS samples (a). Orientation map of as deformed alloys HPS γ ≈ 15(b), HPS γ ≈ 20(c) and HPT γ ≈ 200(d). Grain size distributions of the as deformed alloys (e).

KAM maps (Figure 3 (b-c)) show that small misorientations (angle <10°) are present within the grains for all samples, this can be directly observed on orientation maps in Figure 2 or thanks to the misorientation angle distribution displayed in Figure 3(e). The corresponding calculated dislocation densities gives $2.7\text{x}10^{15}$, $3.1\text{x}10^{15}$ and $4.2\text{x}10^{15}$ respectively for HPS γ ≈ 15, γ ≈ 20 and HPT γ ≈ 200. That shows an increase in dislocations density with the increasing applied deformation.

The misorientation distributions (Figure 3(e)) show a large fraction of high angle grain boundaries for all deformations, as expected after severe plastic deformation [53,54]. The only difference between samples is a slight increase in the average misorientation angle with the applied increased deformation.

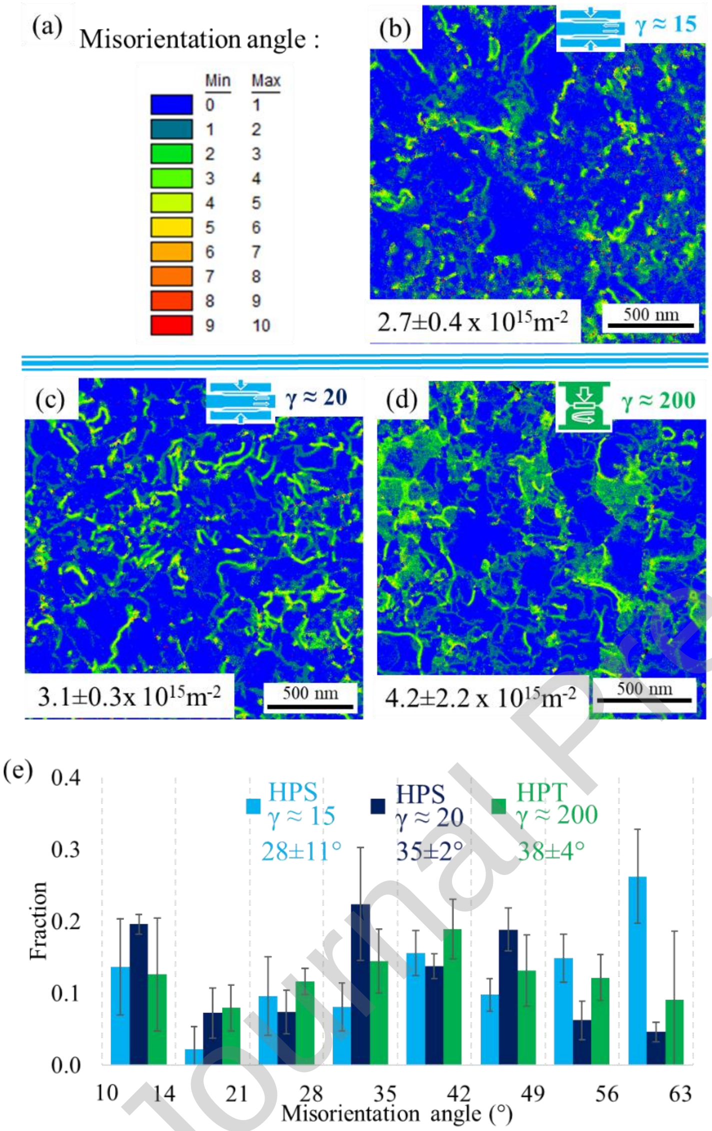

Figure 3:KAM maps (a) for as deformed sample by HPS γ ≈ 15 (b), HPS γ ≈ 20 (c) and HPT γ ≈ 200 (d). Misorientation angle distribution for HPT and HPS deformed alloys (e).

The material was in solid solution state before deformation, however, as shown on the Z contrast STEM HAADF images (Figure 4(a-c)), some chemical heterogeneities are observed in the as deformed states. After both HPS and HPT deformation, some segregations (arrowed on Figure 4(a-c)) and few nanoscaled precipitates (circled in Figure 4(a)) along boundaries can be observed. STEM Z contrast indicates that they contain a significant amount of solute with a higher atomic number than Al (Zn, Cu or Zr).

This is consistent with our previous work [5] where segregations along boundaries of 5at% of Mg and 7at% of Zn were quantified by atom probe tomography (APT). Precipitates analyzed by APT in the as HPT material [5] consisted in two populations of precipitates identified as intragranular GPzones (<1nm radius) and intergranular η’/η precipitates (around 10nm radius) with composition of 17.6±4.3at% of Zn and 7.3±4.3at% of Mg for GPzones and 24.3±1at% of Zn and 15.1±0.9at% of Mg for η’/η. Similarly, we carried out an APT analysis of the HPS $\gamma \approx 15$ samples (presented in supplementary material S1) and the results show exactly the same microstructure with the two population of precipitates and with the same composition.

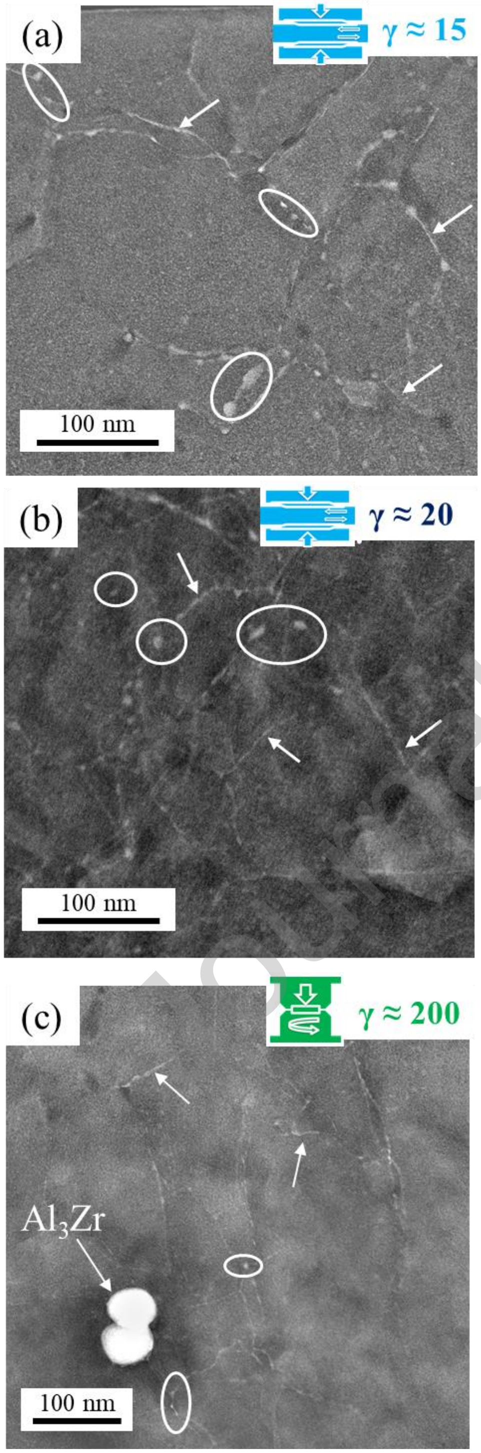

Figure 4: STEM HAADF images of as deformed alloys: HPS $\gamma \approx 15$ (a), HPS $\gamma \approx 20$ (b), HPT $\gamma \approx 200$ (c).

The precipitate size and fraction were quantified by SAXS measurements. Size distributions of precipitates in the HPS (γ ≈ 15, γ ≈ 20) and HPT (γ ≈ 200) deformed alloys are displayed in Figure 5.

The precipitate size distributions from the deformed alloys (Figure 5) can be divided in two populations: the first population shows radiuses between 0.4 and 1 nm (presumably GPzones) and the second encompasses radiuses between 1.5 and 4 nm but with a much lower volume fraction, that we will consider in the following to be η'/η precipitates. The most deformed alloy (HPT) shows a third population with radiuses between 5 and 10nm. In addition to this third population, it can be noted that the precipitation fraction seems more important in the case of HPT deformed alloy. Besides, it is important to note that the SAXS set up used in this study allows the observation of precipitates with a size <10nm, larger precipitates are therefore not considered here.

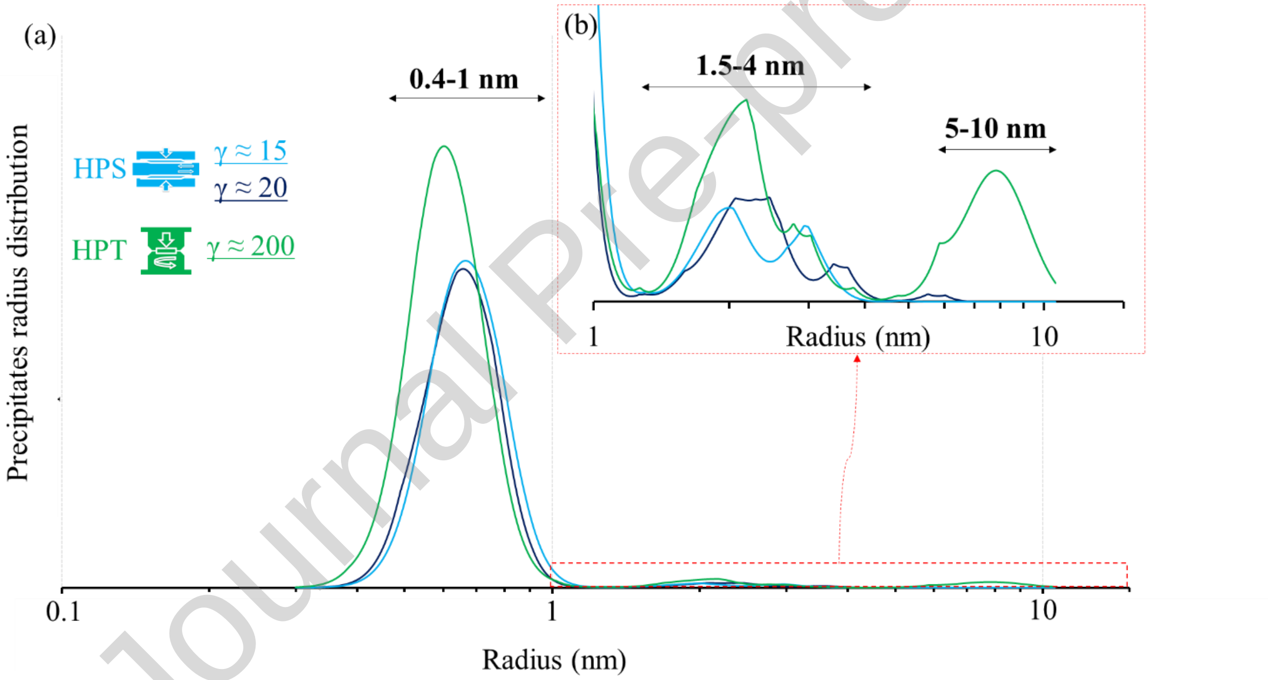

Figure 5: Precipitate size distribution calculated from SAXS data fitting for the HPS (blue lines) HPT (green line) deformed materials at 25°C.

Correlation between STEM images (Figure 4) and APT results (supplementary material S1) with SAXS analyses (Figure 5), shows that the population of size <1nm may correspond to the intragranular GPzones, and that populations between 1.5 and 10 nm to intergranular precipitates. In addition, STEM results clearly show numerous precipitates with a size larger than the SAXS detection limit (10nm).

These first results demonstrate that deformation by HPS and HPT of the AlZnMgCu alloy give rise to similar microstructures, with an average grain size below 1µm, a high dislocation density, segregations and precipitation along defects (especially GBs) but also intragranular precipitation. Nevertheless, there are few noticeable differences: i) a less pronounced grain refinement for the γ ≈ 15 HPS material, ii) a higher fraction of GPzones after deformation by HPT, iii) a higher volume fraction of intergranular precipitates (size from 1.5 to 10 nm) after HPT deformation. These slight differences may have an influence on mechanical properties but also on the post deformation ageing behavior.

3.2. *Thermal stability during post deformation annealing*

Observations of the progressive microstructure evolution during ageing could show if slight differences between HPS and HPT microstructures significantly influence the overall thermal stability. Besides, for precipitation, the ageing temperature has to be carefully selected to be able to follow the first stage of precipitation in these deformed materials. Therefore, a preliminary study of precipitates evolution has been done by *in situ* SAXS with a temperature ramp before isothermal treatments. To guarantee a sufficient acquisition time, a low heating rate of 0.5°C/min was used. The calculation of SAXS data collected during the heating ramp allowed to represent the precipitate size distributions (PSD) as a function of temperature in contour plots for HPS materials in Figure 6(a, b).

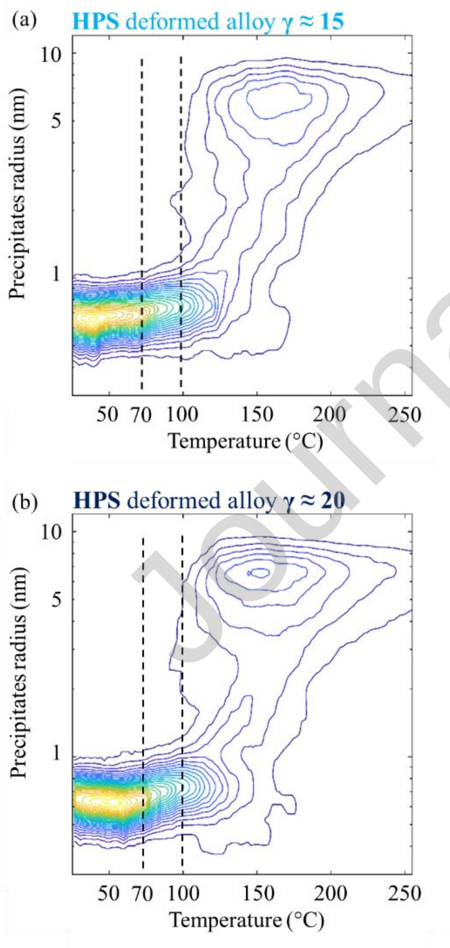

Figure 6: Precipitates size distribution estimated from SAXS data fitting during an in situ heating at 5°C/min from 20 to 250°C on HPS deformed alloy: (a) γ ≈ 15 and (b) γ ≈ 20.

In the two HPS deformed materials (Figure 6(a, b)), precipitate size distributions are very similar. At the beginning (20-50°C) GPzones are stable with only a very slight increase of the mean radius. At 70°C, a significant growth is visible, together with a slight decrease of the volume fraction. Between 80 and 100°C, larger precipitates start to grow, which can be identified as η'/η. Above 100°C, there is an increase of both the η'/η mean radius and volume fraction. At the same time, the volume fraction and mean size of GPzones continues to decrease. These evolutions are very similar to that of the alloy deformed by HPT and distinct from the much more continuous evolution in the undeformed alloy [5]. Finally, comparing to the thermal behavior of HPT samples, the main difference is that the formation of the η'/η precipitates starts at a slightly higher temperature (75°C and 85°C for HPT and HPS respectively).

Thus, similarly to HPT samples, a significantly lower aging temperature is required to control the precipitation kinetic as compared to coarse grained materials for which the classical T6 thermal treatment is typically between 120 and 160°C. Hence, in the following, two temperatures have been selected for isothermal treatments, as indicated by dashed lines in Figure 6: 70°C, which is the temperature just before the evolution of GPzones and the formation of the η'/η precipitates, and 100°C, which is the temperature where these η'/η precipitates start to grow.

3.3. *Precipitation kinetics during isothermal ageing*

To follow the evolution of PSDs during isothermal heat treatments at 70°C and 100°C, the average precipitate sizes of the two main precipitate families, and their respective volume fraction evolutions extracted from the SAXS data were plotted (Figure 7 and Figure 8).

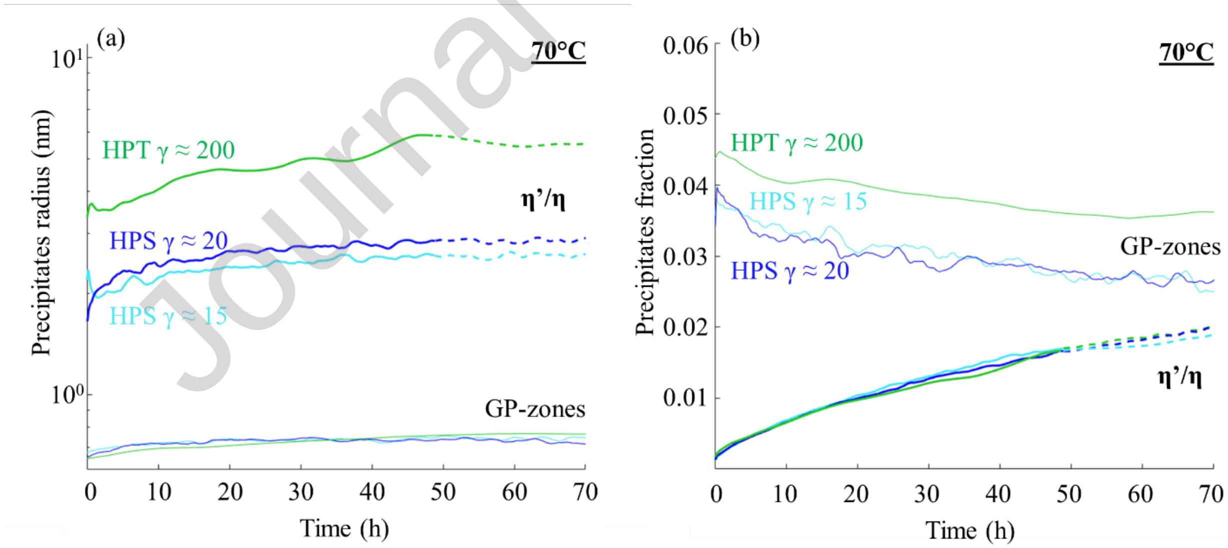

Figure 7 : Precipitate size (a) and fraction evolution (b) estimated from SAXS data fitting during in situ heating at 70°C on HPS (blue) and HPT (green) deformed alloys. Thin lines correspond to GPzones and thicker lines to η'/η. Dashed lines correspond to the uncertainty of the evolutions due to the SAXS detection limit.

At 70°C, the evolution of GPzones is similar in the three materials (HPT, HPS γ ≈ 15 and γ ≈ 20), with limited evolution of the radius up to 0.5nm and a slight decrease of volume fraction with time which can be related to the growth of larger precipitates, as observed at 100°C during ramp heating (Figure 6). Indeed, in the three materials, there is an increase in η'/η precipitate volume fraction. It seems that their radius also increases, even if it is close to the detection limit of SAXS (10nm). This could explain why there is a stabilization of the curves at the end of the ageing and not a continuous increase in size but also in fraction (dashed lines on Figure 7 represent the uncertainty of the evolutions due to the SAXS detection limit). The only difference between the three materials is the average radius size of the η'/η precipitates. Indeed, it seems that the larger size of precipitates is obtained in the HPT alloy (from 2 (γ ≈ 15 by HPS) to 2.5 (γ ≈ 20 by HPS) and to 5 nm (γ ≈ 200 by HPT after 70h)).

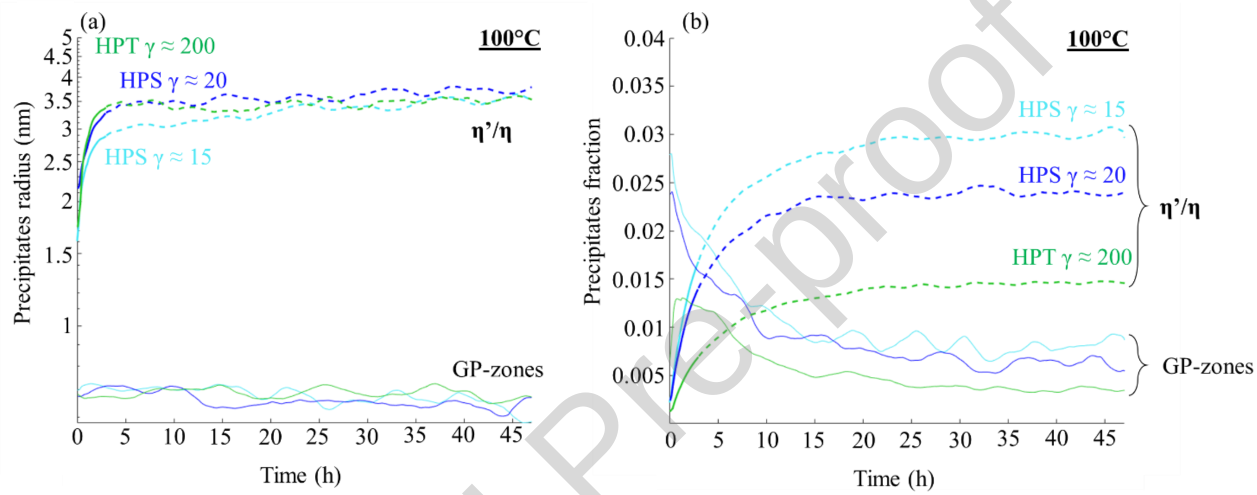

Figure 8 : Precipitate size (a) and volume fraction evolution (b) estimated from SAXS data fitting during in situ heating at 100°C on HPS (blue) and HPT (green) deformed alloys. Thin lines correspond to GPzones and thicker lines to η'/η evolutions. Dashed lines correspond to the uncertainty of the evolutions due to the SAXS detection limit.

At 100°C, the GPzones mean radius remains rather constant, and their fraction clearly decreases for all samples. The fraction of η'/η precipitates rapidly increases together with their size during the three first hours of the treatment, and then stabilizes. Besides, the more the material is deformed, the lower the volume fraction of η'/η precipitates. However, again with a detection limit near 10 nm, a non-negligible fraction of precipitates could be missed and that would change the tendency as reported in [5].

To confirm these analyses with direct observations, and also to see if precipitates of radius size >10nm are present, STEM-HAADF imaging has been performed after 70h at 70°C (Figure 9(a,c,e)) and after 48h at 100°C (Figure 9(b,d,f)).

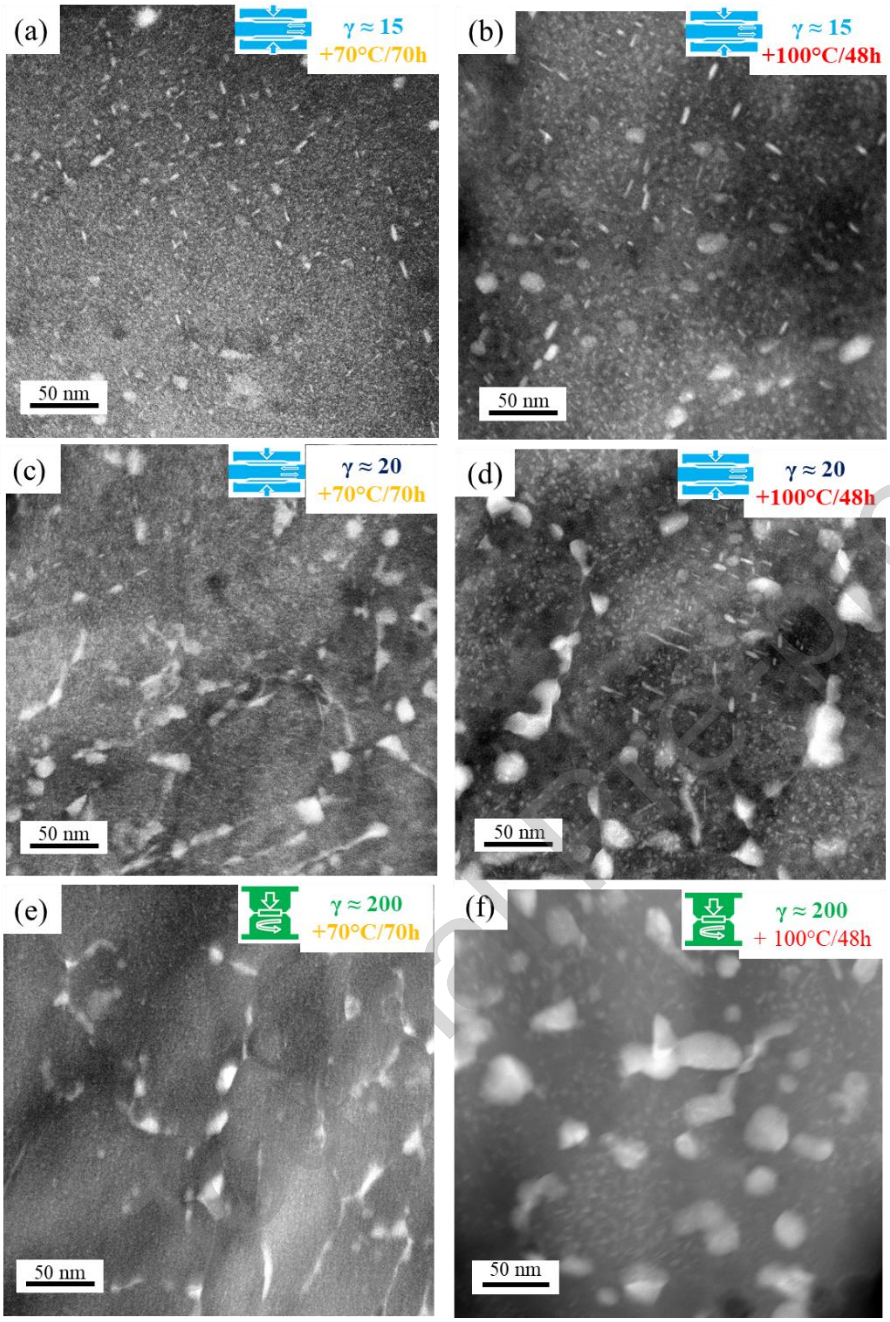

Figure 9 : STEM-HAADF images of HPS deformed alloy: γ ≈ 15(a, b) and γ ≈ 20 (c, d) and of HTP deformed alloy (e, f) annealed 70h at 70°C (a, c, e) and 48h at 100°C (b, d, f).

After 70°C/70h (Figure 9(a, c, e)), precipitates of about 10 nm are observed. They are localized on crystalline defects, mainly along grain boundaries. It should be noted that a small fraction of precipitates with radius between 10 and 15 nm for materials deformed with γ ≈ 20 by HPS and with γ ≈ 200 by HPT are also observed. Thus, even a relatively low thermal treatment allows nucleation and growth of a high density of precipitates. A second precipitates population is observed, located inside grains with a size of the order of 1 nm. These observations confirm the SAXS data and confirm the fact that SAXS experiments do not detect precipitates with a radius greater than 10 nm.

Images of the deformed alloys after 100°C/48h (Figure 9(b, d, f)) reveal numerous intergranular precipitates with radius up to 20 nm, thus larger than after 70°C/70h, as well as intragranular precipitates which are also larger than after 70°C thermal treatment. Near grain boundaries, an intragranular area without precipitates clearly appear identified as a precipitate-free-zones (PFZ). A non-negligible amount of precipitates with size above the SAXS measured range are observed by TEM, which can explain the difference in size distribution between the two techniques. It also highlights an inhomogeneous microstructure for the least deformed material ($\gamma \approx 15$ by HPS) compared to the two others deformed materials. Indeed, there are zones with smaller precipitates homogeneously distributed in the matrix, and zones with smaller intragranular precipitates and bigger intergranular precipitates.

These differences could have an influence on the evolution of grain size during ageing; therefore, orientation maps were performed after these heat treatments and are presented in Figure 10.

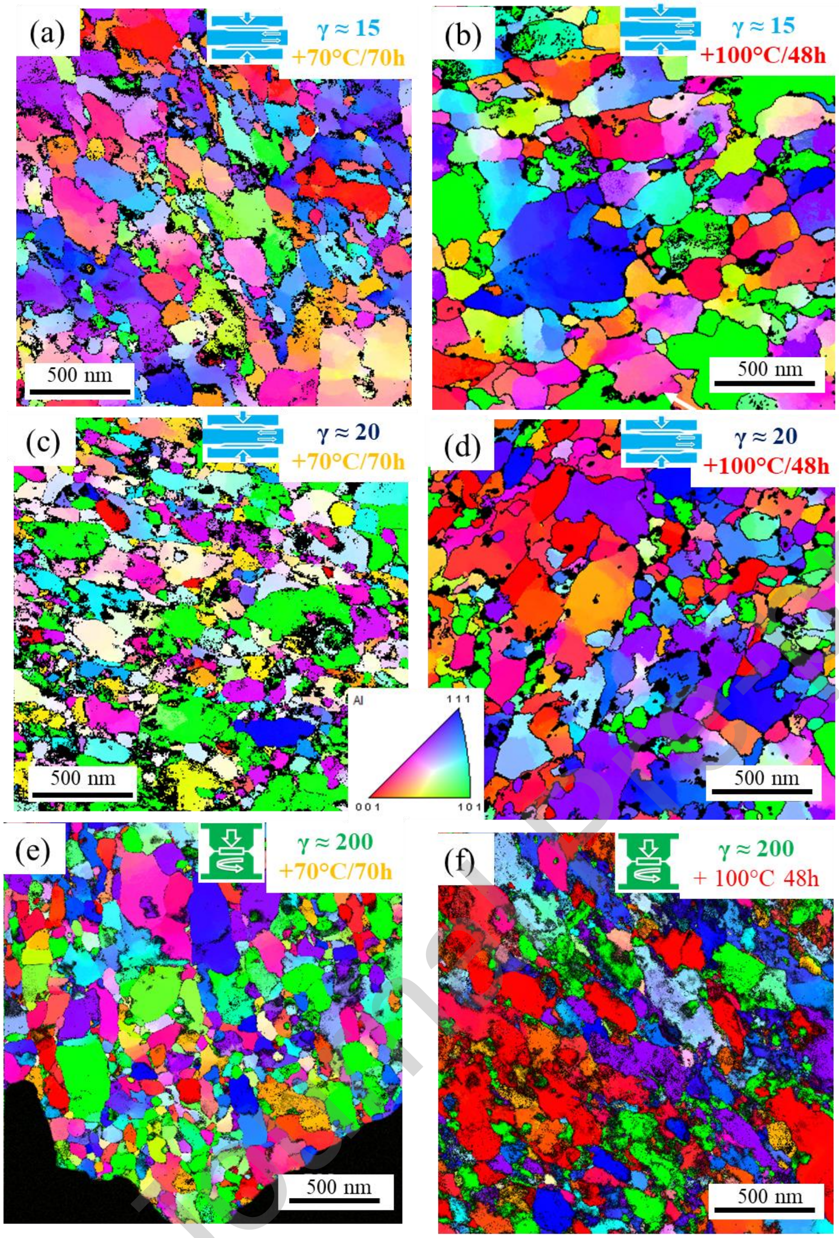

Figure 10 : TEM orientation maps of HPS deformed alloy: γ ≈ 15(a, b) and γ ≈ 20 (c, d) and of HTP deformed alloy (e, f) annealed 70h at 70°C (a, c, e) and 48h at 100°C (b, d, f).

The orientation maps of the deformed alloys after 70h at 70°C (Figure 10(a, c, e)) show that the grain size remains relatively stable for all samples. However, it seems that the higher was the deformation, the smaller the grain size after 70°C treatment. And even after 48h at 100°C, the orientation maps of the deformed materials (Figure 10(b, d, f)) show that a grain size smaller than 600 nm is retained.

Grain size distributions (in surface fractions) were extracted from these orientation maps and are plotted in Figure 11.

These results show that the average grain size distribution is shifted towards smaller values for all materials after 70h at 70°C as compared to the as-deformed state: from 520 to 380 nm for γ ≈ 15, from 220 to 170 for γ ≈ 20 and from 210 to 150 for γ ≈ 200. However, the grain size distribution of the least deformed material shows a significant reduction of grains with a diameter smaller than 170 nm as compared to the two others materials. This indicates that some grain growth occurred in the alloy deformed by HPS γ ≈ 15, while partial recrystallization occurred in the two others materials (HPS γ ≈ 20 and HPT γ ≈ 200).

After annealing at 100°C, the mean grain size is 540 ± 190 nm for HPS γ ≈ 15, which is larger than that of the as-deformed material, evidencing some grain growth. However, for the material deformed by HPS γ ≈ 20, the grain size is relatively stable (from 220 ± 20 to 230 ± 20 nm), showing surprisingly a higher stability. Last, the material deformed by HPT γ ≈ 200 exhibits a significant decrease in grain size from 210 ± 50 to 170 ± 30 nm.

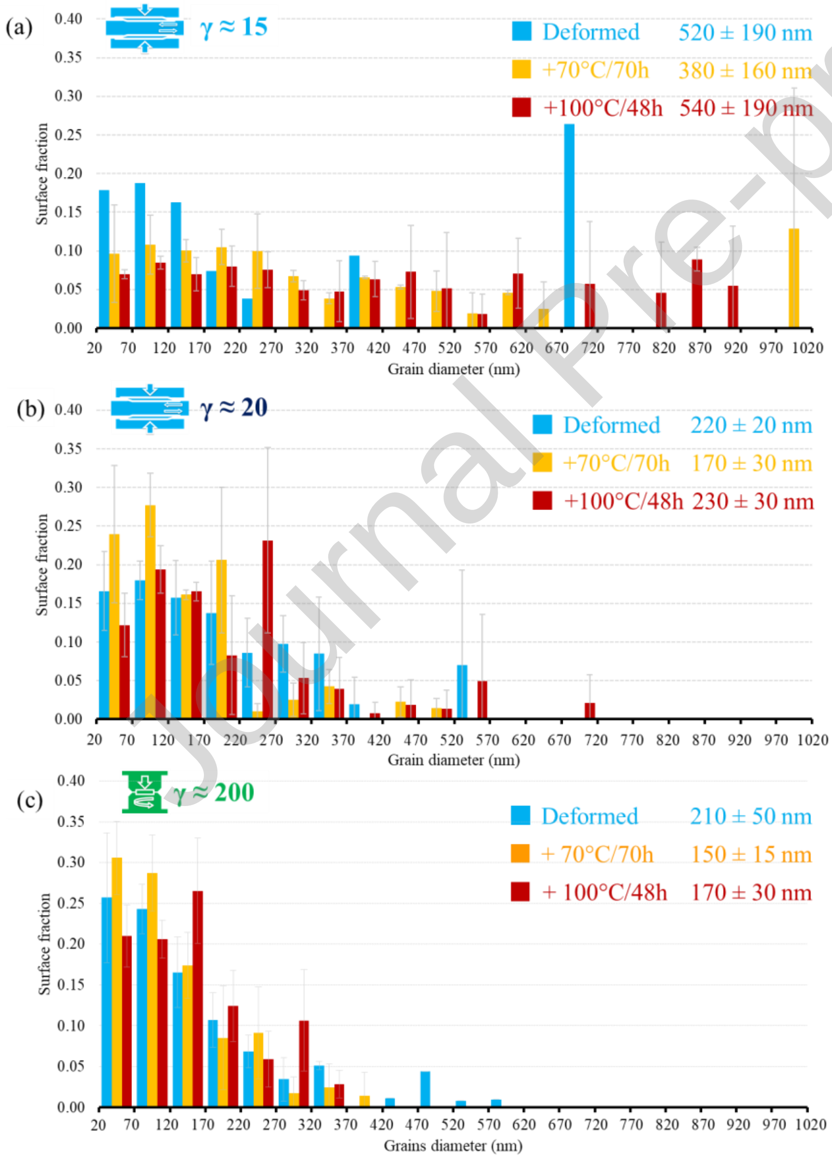

Figure 11 : Grain size distributions of HPS (a, b) and HPT (c from [5]) deformed materials before (blue) and after annealing at 70°C/70h (yellow) and 100°C/48h (red)

These results show that a thermal treatment during 70h at 70°C leads to a grain growth for the least deformed sample and that recovery or at least partial recrystallization occurred for the most deformed materials. In supplementary material (S2), the misorientation angle distributions for HPS samples show a decrease in fraction of small misorientation (<14°) and an increase of the average misorientation angle. In contrary, for the HPT deformed sample, there is an increase in fraction of the small misorientations and a decrease in the average misorientation angle. That could show that the mechanism which lead to a decrease in average grain size is different for HPS and HPT sample. The decrease in small misorientation in HPS material could suggest recovery and their increase in HPT material to a partial recrystallization (not happening in the whole material) explained by a re-organization of dislocations in dislocation walls.

KAM maps (Supplementary materials S3 and [5]) show that this decrease in small misorientations (<10°) for all samples after both annealing can be attributed to a decrease in dislocation density presented in Table 2 (dislocation densities were calculated using eq. (2)).

Dislocation densities ($\times 10^{15}$ m^{-2})	**As deformed**	**After 70°C/70h**	**After 100°C/48h**
HPS $\gamma \approx 15$	2.7 ± 0.4	2.0 ± 0.1	2.0 ± 0.7
HPS $\gamma \approx 20$	3.1 ± 0.3	2.9 ± 0.3	1.8 ± 0.1
HPT $\gamma \approx 200$	4.2 ± 2.1	2.8 ± 1.3	2.8 ± 0.7

Table 2 : Dislocation densities estimated from KAM maps for as deformed and after ageing materials.

Finally, after annealing during 48h at 100°C, the behavior of the materials changes. For the least deformed material ($\gamma \approx 15$), the increase of the average grain size suggests a grain growth more pronounced than during 70°C treatment, even if it remains limited. For the $\gamma \approx 20$ deformed material, a stabilization of the grain size is observed. Last, for the most deformed sample ($\gamma \approx 200$), there is still a grain size reduction even if it is less pronounced than after annealing at 70°C. Unexpectedly these different behaviors show that the more the material is deformed, the higher is its thermal stability.

3.4. *Mechanical properties*

The tensile curves of HPT and HPS deformed materials are presented in Figure 12.

The tensile curve of the as deformed materials exhibits a yield stress around 820 MPa for $\gamma \approx 15$, around 825 MPa for $\gamma \approx 20$ and 870 MPa for $\gamma \approx 200$. The cutting direction of the HPS samples seems to have no significant influence on the yield stress. As expected, the more the material is deformed, the higher is the yield stress. Concerning the elongation to failure, HPS samples that were cut in the parallel direction and HPT samples both exhibit a value around 9±3%. However, HPS samples cut in the perpendicular direction exhibits a significantly lower elongation: around 5±2% for $\gamma \approx 15$ and $\gamma \approx 20$ HPS samples.

Annealing at 70°C during 70h leads to a decrease of approximatively 60 MPa of the yield stress for the HPS $\gamma \approx 15$ sample and an increase of ~ 45 MPa and ~ 80 MPa for HPS $\gamma \approx 20$ and HPT γ

≈ 200 samples respectively. For all materials, there is a decrease (< 2%) in elongation to failure (Table 3). The HPS samples cut in the perpendicular direction still exhibit a lower elongation compared to the parallel one.

After annealing at 100°C during 48h, the two HPS alloys exhibit the same behavior with a decrease in yield stress: from 820 to 725 MPa for HPS $\gamma \approx 15$ and from 825 to 770 MPa for HPS $\gamma \approx 20$. In contrast, the material deformed by HPT shows an increase in yield stress of 20 MPa after annealing at 100°C. It is however a lower yield stress as compared to the 70°C treatment.

For all materials, the 100°C heat treatment leads to a slight increase of the elongation to failure, or at least a stabilization.

It could be noted that there is an influence of the tensile direction (parallel or perpendicular to the HPS direction) on the final yield stress. Indeed, differences of 26 MPa and 9 MPa after annealing at 70°C are observed for $\gamma \approx 15$ and $\gamma \approx 20$ deformed alloys respectively. And these differences are larger after the 100°C heat treatment: 48 MPa for $\gamma \approx 15$ and 22 MPa for $\gamma \approx 20$ deformed alloys.

In the data summary of Table 3, it is important to note that extremely high ultimate tensile strength (UTS) are shown: 960 ± 20MPa obtained after HPT and 889 ± 38MPa after HPS followed by annealing at 70°C.

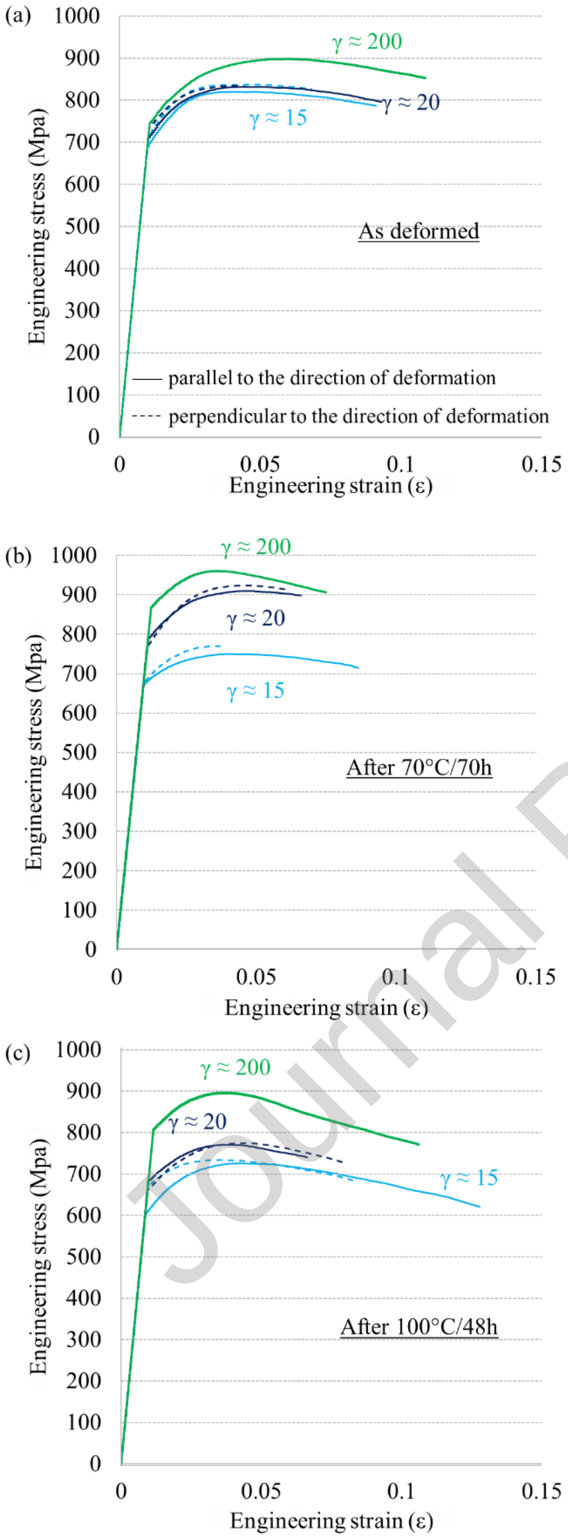

Figure 12: (a) Tensile curves of HPT deformed material (green) and HPS deformed material (blue): dashed line for sample cut perpendicular to the deformation direction and solid line for sample cut in parallel to the deformation direction. (b)after annealing at 70°C/70h and (c) after 100°C/48h.

Table 3 : Yield stress, ultimate tensile stress and elongation to failure for as deformed HPS and HPT materials and after annealing at 70°C/70h and at 100°C/48h. Pa is for parallel to the deformation direction and Pe for perpendicular (see Figure 1 for details)

		Yield stress 0.2%			**Elongation**			**UTS**		
		As deformed	+ 70°C-72h	+ 100°C-48h	As deformed	+ 70°C-72h	+ 100°C-48h	As deformed	+ 70°C-72h	+ 100°C-48h
γ ≈ 15 HPS	Pa	813 ± 17	740 ± 50	704 ± 38	9.1 ± 2	6.7 ± 3.5	10.8 ± 3.6	817 ± 15	752 ± 48	717 ± 45
	Pe	821 ± 15	766 ± 15	752 ± 17	5.9 ± 1.2	4.5 ± 1.5	9.5 ± 1.9	826 ± 16	775 ± 20	758 ± 13
γ ≈ 20 HPS	Pa	826 ± 19	877 ± 34	763 ± 49	8.9 ± 1.3	6.3 ± 1.7	8.3 ± 2.2	836 ± 22	889 ± 38	802 ± 26
	Pe	824 ± 27	868 ± 16	785 ± 35	3.9 ± 0.3	3.5 ± 1.2	5.9 ± 1.5	829 ± 26	875 ± 14	800 ± 28
γ ≈ 200 HPT		869 ± 22	947 ± 15	893 ± 13	9.1 ± 2.9	7.1 ± 0.6	9.9 ± 1.4	917 ± 21	953 ± 9	902 ± 13

4. Discussion

4.1. *Deformation induced microstructure*

In both cases, during SPD by HPS or HPT, a significant grain refinement with high density of intragranular defects resulting in local lattice distortions was achieved. A mean grain size of 520 ± 190 nm, 220 ± 20 nm and 210 ± 50 nm was obtained by HPS $\gamma \approx 15$, HPS $\gamma \approx 20$ and HPT $\gamma \approx 200$ respectively, These mean grain sizes are significantly larger than those reported in the literature for similar alloys (typically 100nm) [55,56]. However, in these prior studies, grain sizes were measured using TEM images or XRD diffraction where every boundary, even with misorientations smaller than 10°, are considered. In the present work, ACOM automated crystal orientation mapping was used, and only HAGBs were considered similarly to the Transmission Kikuchi Diffraction technique [30]. Thanks to such precise evaluation, it has been possible to point out significant differences between the AlZnCuMg alloy deformed by HPS $\gamma \approx 15$ and HPS $\gamma \approx 20$ (grain sizes differ from a factor of two) while grain size distributions are very similar for the material deformed by HPS $\gamma \approx 20$ and HPT $\gamma \approx 200$. This clearly indicates that the critical shear strain level leading to a saturation of the grain size refinement [57] is close to $\gamma \approx 20$. This value is relatively low as compared to pure materials due to the high concentration of solute atoms in the solutionized AlZnCuMg alloy, that reduce dynamic recovery mechanisms.

This reduction of grain size can explain partially the very high yield stress that was obtained. Partially because even if the average grain sizes of materials deformed by $\gamma \approx 20$ (HPS) and $\gamma \approx 200$ (HPT) are very close, the mechanical behavior of $\gamma \approx 20$ (HPS) material is closer to the material deformed by $\gamma \approx 15$ (HPS). There is therefore the presence of other hardening mechanisms, this might be the fraction of HAGBS (higher for HPT deformed alloy) or the precipitation (faster in HPT deformed alloy).

After SPD by HPS or HPT, GPzones and η'/η precipitates were detected by SAXS and TEM. These precipitates also contribute to yield stress. Such dynamic precipitation may result from an enhanced atomic mobility at room temperature, driven by strain induced vacancies [21,58,59] and solute drag by dislocations and GBs. Crystalline defects may promote solute transport but also act as segregation and/or nucleation site for precipitates (both during deformation and natural aging) and thus play an important role in the spatial redistribution of solutes. During deformation, moving dislocations may drag solute atoms and transport them to grains boundaries [21], grains boundaries motion may sweep solute atoms (snowplow effect [60]) and vacancies may also drag solutes with a positive binding energy toward GBs [20]. These three possible mechanisms, eventually combined, promote the formation of Zn, Mg and Cu segregations as observed by TEM in the present work but also reported in other systems [20,61]. They also promote the precipitation of GP zones and η'/η precipitates detected by SAXS and TEM in the AlZnCuMg alloy deformed by HPS or HPT.

In the material deformed by HPS $\gamma \approx 15$, a smaller mean precipitates size was measured as compared to others materials (HPS $\gamma \approx 20$, HPT $\gamma \approx 200$), but with a similar precipitate volume fraction.

Finally, despite the different deformation processing and the large difference in applied strain, the microstructure of the material deformed by HPS is very close from the material deformed by HPT at $\gamma \approx 200$. Their slight differences can result from multiple origins (precipitates size or fraction, fraction of segregations, fraction of HAGBs). These are promising results that will allow to easily transfer the knowledge acquired from HPT to HPS processing in the perspective of industrialization.

4.2. Evolution of nano-structures during ageing

Several works in the literature show that severe plastic deformation affects the precipitation sequence of alloys such as Al-Zn-Mg-Cu [5,19,62–65]. In this work, TEM and SAXS analyses indicate both that for all deformed materials, a bi-modal precipitate size distribution is achieved even during low temperature treatment. For other severely deformed aluminum alloys, a faster kinetics has also been reported and has been attributed to: -i)- strain induced excess vacancy concentration; -ii)- heterogeneous nucleation on structural defects; -iii)- accelerated diffusion along crystalline defects; -iv)- solute drag by motion of defects during their recovery.

STEM observations show that this bi-modal precipitate size distribution results from a population of large precipitates mainly located on grain and sub-grain boundaries, combined with a finer-scale intragranular population. Thanks to the SAXS data, a quantitative comparison between HPS and HPT deformed materials was possible. During low isothermal ageing at 70°C (Figure 7), the behavior of GPzones is similar in all materials with a progressive partial dissolution of them. Their size and volume fraction are also quantitatively similar in all materials. The evolution of η’/η precipitates (nucleation and growth) also follows a similar trend in all materials. with only a slight difference in size: the more intense was the deformation, the larger the size of the η’/η precipitates. At 100°C, the global evolution of the GPzones is similar to observations done in all deformed materials at 70°C but with a faster decrease in volume fraction. Regarding η’/η precipitates, their nucleation and growth is significantly faster as compared to the 70°C treatment. In our measurements, the size and the volume fraction quickly reach a plateau but it is simply related to the detection limit of the SAXS technique (about 10 nm). Thanks to STEM images, a significant fraction of larger precipitates (radius > 10 nm) could be evidenced in all materials. Detailed observations revealed that, during ageing at 100°C, these η’/η precipitates are located on defects (mainly GBs) where they could grow quickly.

The difference in the fraction of η’/η precipitates between HPS and HPT materials could be explained by the grain size. Indeed, if the grain size is smaller (HPT) then the fraction of GBs is higher, so there are more heterogeneous nucleation sites and more accelerated diffusion paths.

The initial grain size has therefore an influence on the precipitation, but as shown by our TEM observations (ACOM, Figure 10 and Figure 11) precipitates also affect the grain size evolution during aging. Three different behaviors have been observed depending on the deformation level:

i) In the sample deformed by HPS $\gamma \approx 15$ a significant grain growth was observed during annealing at 70°C or 100°C as expected.
ii) In the sample deformed by HPS $\gamma \approx 20$, annealing at 70°C leads to a mean grain size reduction, while at 100°C it is relatively stable. Thus, annealing at low temperature (70°C) seems to promote a partial recrystallization, but at 100°C it is most probably quickly offset by grain growth.
iii) For the sample deformed by HPT $\gamma \approx 200$, a significant grain size reduction was measured after annealing at both 70°C and 100°C. Thus, recrystallization occurred with probably more nuclei and eventually a more stable ultrafine grain structure.

Such grain size reduction due to recrystallization or partial recrystallisation after SPD has been scarcely reported in the literature [66,67]. The driving force is the high density of crystalline defects and the main mechanism is probably driven by re-organization of dislocations in cell-walls and the transformation of sub-grain boundaries into high-angle grain boundaries via the absorption of dislocations [66]. If the mobility of GBs is sufficiently high (such as in commercially pure alloys), these new grains quickly grow and are eventually difficult to detect but in the AlZnCuMg alloy segregations and precipitates (Figure 4), pin GBs and reduce their mobility. Since heterogeneous precipitation along intragranular dislocations was not observed, this suggests that dislocation recovery occurred faster than precipitate nucleation and that partial recrystallization occurred in the early stage of annealing. The larger the dislocation density and the fraction of LAGBs the stronger this recrystallization mechanism will be, explaining the observed influence of the strain level.

Grain growth is more pronounced for the least deformed sample (HPS $\gamma \approx 15$). This might be explained by a lower driving force for recrystallization that gives rise to less grain nuclei but also to a relatively high GB mobility due to a low segregation level and rather limited dynamic precipitation (weaker GB pinning).

In conclusion, the stabilization of the microstructure after deformation depends on the synergy between the re-organization of dislocations, precipitation and mobility of grain boundaries (grain growth). This synergy depends on the dislocations and GBs density as well as on the distribution of solutes and precipitates in the deformed state. In the present AlZnCuMg alloy, it seems that a minimum shear deformation of $\gamma = 20$ is required to obtain a stable microstructure up to 100°C.

4.3 Relationship between process, structure and mechanical properties

All microstructural features (GBs, dislocations, solute atoms, precipitates) have an influence on the mechanical behavior of the UFG AlZnCuMg alloy. As shown in our previous work [5] it is however complex to decorrelate each contribution because of the complexity of microstructures. For example, if the contribution of homogeneously dispersed intragranular precipitates is well established, the role of intergranular precipitates and precipitate-free-zones observed after annealing along boundaries is difficult to evaluate. Similarly, classical models established to account for the contribution of dislocations or of grain boundaries do not consider the influence of segregations or of the specific distribution (dislocation cell walls, grain size distribution).

However, our previous work [5] shows also that despite this complexity, grain boundaries and intragranular misorientations contribute to more than two-thirds of the yield stress while the rest is provided by precipitates and the solid solution.

Finally, HPS has shown the potential to reach comparable microstructures as those obtained by HPT. At the higher deformation by HPS very similar mechanical properties was obtained as compared to the HPT. The yield strength after deformation is exceptional for aluminum alloys (>800MPa), and one can notice that even at comparable grain sizes, others aluminum alloys do not reach this level. For example: AA6060, AA6061, Al-3.3Mg, Al-5.5%Mg, Al-1.7%Cu, Al-2%Fe reached yield strength <700MPa, an Al-3%Cu-1%Li reached 700MPa and an Al-8.8%Mg

735MPa [6,68–71]. Finally, in most aluminum alloys the maximum yield strength after HPT is <800MPa [72].

Moreover, the obtained microstructure allows to stabilize these good mechanical properties after annealing, even sometimes to increase them to reach values of UTS >900MPa. These results on this HPS deformation process are thus very promising.

5 Conclusions

In conclusion, like in the AlZnMgCu material deformed by HPT [5], HPS processing leads to microstructures where complex interactions between precipitation, grain growth and recrystallization occur. These features were investigated before and after annealing at low temperature (70°C and 100°C). Complementary characterization techniques (TEM-ACOM, STEM-HAADF and SAXS) allowed a precise comparison between microstructures after HPT and HPS. A special emphasis was given on competing mechanisms leading to structural evolutions during aging and on the relationship between final microstructures and the mechanical behavior.

The main findings of this study are:

- Even if the plastic strain imposed by HPS is, at least, 10 times lower than during HPT, very similar microstructures can be obtained. This led to a yield stress higher than that achieved after classical precipitation treatment of the coarse-grained material.
- The coexistence of small precipitates (GPzones) and η’/η precipitates with approximatively the same evolutions during ageing for HPS and HPT processed samples are observed.
- For both processes (HPS and HPT), an exceptional yield strength was obtained (>800MPa). After aging, it ranges from 750 to 950MPa, a level only scarcely reached in aluminum alloys processed by SPD.

Finally, similar microstructures were achieved by HPS and HPT, always with a good thermal stability thanks to the competition between precipitation, recrystallization and recovery. Thus, the HPS process can be envisioned as a continuous process promising for large scale production and potential industrialization of very high yield strength aluminum alloys.

Acknowledgements

Both the Agence Nationale de la Recherche (ANR) and the joint CNRS-JSPS 2017 summer program for the support to the trans-national collaboration are gratefully acknowledged for financial support (PRASA project - ANR-15-CE08-0029). This work was also supported in part by Grant-in-Aids for Scientific Research (S) and (A) from the MEXT, Japan (No. JP26220909 and JP19H00830). HPT was carried out in the International Research Center on Giant Straining for Advanced Materials (IRC-GSAM) at Kyushu University. Our thanks are due to Dr. Yoichi Takizawa of Nagano Forging Co. Ltd. in Japan for HPS processing. This research has benefited from characterization equipments of the Grenoble INP - CMTC platform supported by the Centre of Excellence of Multifunctional Architectured Materials "CEMAM" n°ANR-10-LABX-44-01 funded by the Investments for the Future programme.

Bibliography

[1] A.S. Argon, P. Haasen, A new mechanism of work hardening in the late stages of large strain plastic flow in F.C.C. and diamond cubic crystals, Acta Metallurgica et Materialia. 41 (1993) 3289–3306. https://doi.org/10.1016/0956-7151(93)90058-Z.

[2] H. Mughrabi, H.W. Höppel, Cyclic deformation and fatigue properties of very fine-grained metals and alloys, International Journal of Fatigue. 32 (2010) 1413–1427. https://doi.org/10.1016/j.ijfatigue.2009.10.007.

[3] D. Yuzbekova, A. Mogucheva, R. Kaibyshev, Superplasticity of ultrafine-grained Al–Mg–Sc–Zr alloy, Materials Science and Engineering: A. 675 (2016) 228–242. https://doi.org/10.1016/j.msea.2016.08.074.

[4] R.Z. Valiev, R.K. Islamgaliev, I.V. Alexandrov, Bulk nanostructured materials from severe plastic deformation, Progress in Materials Science. 45 (2000) 103–189. https://doi.org/10.1016/S0079-6425(99)00007-9.

[5] A. Duchaussoy, X. Sauvage, A. Deschamps, F. De Geuser, G. Renou, Z. Horita, Complex interactions between precipitation, grain growth and recrystallization in a severely deformed Al-Zn-Mg-Cu alloy and consequences on the mechanical behavior, Materialia. 15 (2021) 101028. https://doi.org/10.1016/j.mtla.2021.101028.

[6] A. Duchaussoy, X. Sauvage, K. Edalati, Z. Horita, G. Renou, A. Deschamps, F. De Geuser, Structure and mechanical behavior of ultrafine-grained aluminum-iron alloy stabilized by nanoscaled intermetallic particles, Acta Materialia. 167 (2019) 89–102. https://doi.org/10.1016/j.actamat.2019.01.027.

[7] H. Gleiter, Nanocrystalline materials, Progress in Materials Science. 33 (1989) 223–315. https://doi.org/10.1016/0079-6425(89)90001-7.

[8] N.Y.C. Yang, T.J. Headley, J.J. Kelly, J.M. Hruby, Metallurgy of high strength Ni–Mn microsystems fabricated by electrodeposition, Scripta Materialia. 51 (2004) 761–766. https://doi.org/10.1016/j.scriptamat.2003.11.001.

[9] C. Suryanarayana, Non-equilibrium Processing of Materials, Elsevier, 1999.

[10] K. Edalati, A. Bachmaier, V.A. Beloshenko, Y. Beygelzimer, V.D. Blank, W.J. Botta, K. Bryła, J. Čížek, S. Divinski, N.A. Enikeev, Y. Estrin, G. Faraji, R.B. Figueiredo, M. Fuji, T. Furuta, T. Grosdidier, J. Gubicza, A. Hohenwarter, Z. Horita, J. Huot, Y. Ikoma, M. Janeček, M. Kawasaki, P. Král, S. Kuramoto, T.G. Langdon, D.R. Leiva, V.I. Levitas, A. Mazilkin, M. Mito, H. Miyamoto, T. Nishizaki, R. Pippan, V.V. Popov, E.N. Popova, G. Purcek, O. Renk, Á. Révész, X. Sauvage, V. Sklenicka, W. Skrotzki, B.B. Straumal, S. Suwas, L.S. Toth, N. Tsuji, R.Z. Valiev, G. Wilde, M.J. Zehetbauer, X. Zhu, Nanomaterials by severe plastic deformation: review of historical developments and recent advances, Materials Research Letters. 10 (2022) 163–256. https://doi.org/10.1080/21663831.2022.2029779.

[11] Y. Saito, H. Utsunomiya, N. Tsuji, T. Sakai, Novel ultra-high straining process for bulk materials—development of the accumulative roll-bonding (ARB) process, Acta Materialia. 47 (1999) 579–583. https://doi.org/10.1016/S1359-6454(98)00365-6.

[12] V. Segal, V.I. Reznikov, A.E. Drobyshevskii, V.I. Kopylov, Plastic Metal Working by Simple Shear, Matally 1. (1981) 115.

[13] N. Sadasivan, M. Balasubramanian, B.R. Rameshbapu, A comprehensive review on equal channel angular pressing of bulk metal and sheet metal process methodology and its varied

applications, Journal of Manufacturing Processes. 59 (2020) 698–726. https://doi.org/10.1016/j.jmapro.2020.10.032.

[14] A.P. Zhilyaev, T.G. Langdon, Using high-pressure torsion for metal processing: Fundamentals and applications, Progress in Materials Science. 53 (2008) 893–979. https://doi.org/10.1016/j.pmatsci.2008.03.002.

[15] R. Pippan, S. Scheriau, A. Hohenwarter, M. Hafok, Advantages and Limitations of HPT: A Review, Materials Science Forum. 584–586 (2008) 16–21. https://doi.org/10.4028/www.scientific.net/MSF.584-586.16.

[16] J. Gubicza, I. Schiller, N.Q. Chinh, J. Illy, Z. Horita, T.G. Langdon, The effect of severe plastic deformation on precipitation in supersaturated Al–Zn–Mg alloys, Materials Science and Engineering: A. 460–461 (2007) 77–85. https://doi.org/10.1016/j.msea.2007.01.001.

[17] M.A. Afifi, P.H.R. Pereira, Y.C. Wang, Y. Wang, S. Li, T.G. Langdon, Effect of ECAP processing on microstructure evolution and dynamic compressive behavior at different temperatures in an Al-Zn-Mg alloy, Materials Science and Engineering: A. 684 (2017) 617–625. https://doi.org/10.1016/j.msea.2016.12.099.

[18] K. Ma, H. Wen, T. Hu, T.D. Topping, D. Isheim, D.N. Seidman, E.J. Lavernia, J.M. Schoenung, Mechanical behavior and strengthening mechanisms in ultrafine grain precipitation-strengthened aluminum alloy, Acta Materialia. 62 (2014) 141–155. https://doi.org/10.1016/j.actamat.2013.09.042.

[19] A. Deschamps, F. De Geuser, Z. Horita, S. Lee, G. Renou, Precipitation kinetics in a severely plastically deformed 7075 aluminium alloy, Acta Materialia. 66 (2014) 105–117. https://doi.org/10.1016/j.actamat.2013.11.071.

[20] X. Sauvage, N. Enikeev, R. Valiev, Y. Nasedkina, M. Murashkin, Atomic-scale analysis of the segregation and precipitation mechanisms in a severely deformed Al–Mg alloy, Acta Materialia. 72 (2014) 125–136. https://doi.org/10.1016/j.actamat.2014.03.033.

[21] B.B. Straumal, B. Baretzky, A.A. Mazilkin, F. Phillipp, O.A. Kogtenkova, M.N. Volkov, R.Z. Valiev, Formation of nanograined structure and decomposition of supersaturated solid solution during high pressure torsion of Al–Zn and Al–Mg alloys, Acta Materialia. 52 (2004) 4469–4478. https://doi.org/10.1016/j.actamat.2004.06.006.

[22] X. Sauvage, E.V. Bobruk, M.Yu. Murashkin, Y. Nasedkina, N.A. Enikeev, R.Z. Valiev, Optimization of electrical conductivity and strength combination by structure design at the nanoscale in Al–Mg–Si alloys, Acta Materialia. 98 (2015) 355–366. https://doi.org/10.1016/j.actamat.2015.07.039.

[23] Y. Nasedkina, X. Sauvage, E.V. Bobruk, M.Yu. Murashkin, R.Z. Valiev, N.A. Enikeev, Mechanisms of precipitation induced by large strains in the Al-Cu system, Journal of Alloys and Compounds. 710 (2017) 736–747. https://doi.org/10.1016/j.jallcom.2017.03.312.

[24] G. Sha, L. Yao, X. Liao, S.P. Ringer, Z. Chao Duan, T.G. Langdon, Segregation of solute elements at grain boundaries in an ultrafine grained Al–Zn–Mg–Cu alloy, Ultramicroscopy. 111 (2011) 500–505. https://doi.org/10.1016/j.ultramic.2010.11.013.

[25] P.V. Liddicoat, X.-Z. Liao, Y. Zhao, Y. Zhu, M.Y. Murashkin, E.J. Lavernia, R.Z. Valiev, S.P. Ringer, Nanostructural hierarchy increases the strength of aluminium alloys, Nature Communications. 1 (2010) 63. https://doi.org/10.1038/ncomms1062.

[26] R.A. Andrievski, Review of thermal stability of nanomaterials, J Mater Sci. 49 (2014) 1449–1460. https://doi.org/10.1007/s10853-013-7836-1.

[27] K.R. Cardoso, D.N. Travessa, W.J. Botta, A.M. Jorge, High Strength AA7050 Al alloy processed by ECAP: Microstructure and mechanical properties, Materials Science and Engineering A. 528 (2011) 5804–5811. https://doi.org/10.1016/j.msea.2011.04.007.

[28] L.J. Zheng, C.Q. Chen, T.T. Zhou, P.Y. Liu, M.G. Zeng, Structure and properties of ultrafine-grained Al-Zn-Mg-Cu and Al-Cu-Mg-Mn alloys fabricated by ECA pressing combined with thermal treatment, Materials Characterization. 49 (2002) 455–461. https://doi.org/10.1016/S1044-5803(03)00069-X.

[29] L.J. Zheng, H.X. Li, M.F. Hashmi, C.Q. Chen, Y. Zhang, M.G. Zeng, Evolution of microstructure and strengthening of 7050 Al alloy by ECAP combined with heat-treatment, Journal of Materials Processing Technology. 171 (2006) 100–107. https://doi.org/10.1016/j.jmatprotec.2005.06.049.

[30] M.H. Shaeri, M.T. Salehi, S.H. Seyyedein, M.R. Abutalebi, J.K. Park, Microstructure and mechanical properties of Al-7075 alloy processed by equal channel angular pressing combined with aging treatment, Materials & Design. 57 (2014) 250–257. https://doi.org/10.1016/j.matdes.2014.01.008.

[31] Z. Horita, T. Fujinami, M. Nemoto, T.G. Langdon, Equal-channel angular pressing of commercial aluminum alloys: Grain refinement, thermal stability and tensile properties, Metall Mater Trans A. 31 (2000) 691–701. https://doi.org/10.1007/s11661-000-0011-8.

[32] Y.H. Zhao, X.Z. Liao, Z. Jin, R.Z. Valiev, Y.T. Zhu, Microstructures and mechanical properties of ultrafine grained 7075 Al alloy processed by ECAP and their evolutions during annealing, Acta Materialia. 52 (2004) 4589–4599. https://doi.org/10.1016/j.actamat.2004.06.017.

[33] M.V. Markushev, E.V. Avtokratova, S.V. Krymskiy, O.Sh. Sitdikov, Effect of precipitates on nanostructuring and strengthening of high-strength aluminum alloys under high pressure torsion, Journal of Alloys and Compounds. 743 (2018) 773–779. https://doi.org/10.1016/j.jallcom.2018.02.047.

[34] Y. Zhang, S. Jin, P. Trimby, X. Liao, M.Y. Murashkin, R.Z. Valiev, G. Sha, Strengthening mechanisms in an ultrafine-grained AlZnMgCu alloy processed by high pressure torsion at different temperatures, Materials Science and Engineering: A. 752 (2019) 223–232. https://doi.org/10.1016/j.msea.2019.02.094.

[35] R.K. Islamgaliev, N.F. Yunusova, I.N. Sabirov, A.V. Sergueeva, R.Z. Valiev, Deformation behavior of nanostructured aluminum alloy processed by severe plastic deformation, Materials Science and Engineering: A. 319–321 (2001) 877–881. https://doi.org/10.1016/S0921-5093(01)01052-8.

[36] Z. Horita, Y. Tang, T. Masuda, Y. Takizawa, Severe Plastic Deformation under High Pressure: Upsizing Sample Dimensions, Materials Transactions. 61 (2020) 1177–1190. https://doi.org/10.2320/matertrans.MT-M2020074.

[37] C. Xu, Z. Horita, T.G. Langdon, The evolution of homogeneity in processing by high-pressure torsion, Acta Materialia. 55 (2007) 203–212. https://doi.org/10.1016/j.actamat.2006.07.029.

[38] T. Fujioka, Z. Horita, Development of High-Pressure Sliding Process for Microstructural Refinement of Rectangular Metallic Sheets, Mater. Trans. 50 (2009) 930–933. https://doi.org/10.2320/matertrans.MRP2008445.

[39] Y. Takizawa, T. Masuda, K. Fujimitsu, T. Kajita, K. Watanabe, M. Yumoto, Y. Otagiri, Z. Horita, Scaling up of High-Pressure Sliding (HPS) for Grain Refinement and Superplasticity, Metall and Mat Trans A. 47 (2016) 4669–4681. https://doi.org/10.1007/s11661-016-3623-3.

[40] K. Edalati, Z. Horita, A review on high-pressure torsion (HPT) from 1935 to 1988, Materials Science and Engineering: A. 652 (2016) 325–352. https://doi.org/10.1016/j.msea.2015.11.074.

[41] K. Edalati, Z. Horita, Correlation of Physical Parameters with Steady-State Hardness of Pure Metals Processed by High-Pressure Torsion, Materials Science Forum. 667–669 (2011) 683–688. https://doi.org/10.4028/www.scientific.net/MSF.667-669.683.

[42] M. Kawasaki, H.-J. Lee, B. Ahn, A.P. Zhilyaev, T.G. Langdon, Evolution of hardness in ultrafine-grained metals processed by high-pressure torsion, Journal of Materials Research and Technology. 3 (2014) 311–318. https://doi.org/10.1016/j.jmrt.2014.06.002.

[43] A.P. Zhilyaev, K. Oh-ishi, T.G. Langdon, T.R. McNelley, Microstructural evolution in commercial purity aluminum during high-pressure torsion, Materials Science and Engineering: A. 410 (2005) 277–280. https://doi.org/10.1016/j.msea.2005.08.044.

[44] Z. Horita, T.G. Langdon, Microstructures and microhardness of an aluminum alloy and pure copper after processing by high-pressure torsion, Materials Science and Engineering: A. 410–411 (2005) 422–425. https://doi.org/10.1016/j.msea.2005.08.133.

[45] C. Xu, T.G. Langdon, Three-dimensional representations of hardness distributions after processing by high-pressure torsion, Materials Science and Engineering: A. 503 (2009) 71–74. https://doi.org/10.1016/j.msea.2008.04.083.

[46] E. Rauch, M. Véron, S. Nicolopoulos, D. Bultreys, Orientation and Phase Mapping in TEM Microscopy (EBSD-TEM Like): Applications to Materials Science, Solid State Phenomena. 186 (2012) 13–15. https://doi.org/10.4028/www.scientific.net/SSP.186.13.

[47] D. Viladot, M. Véron, M. Gemmi, F. Peiró, J. Portillo, S. Estradé, J. Mendoza, N. Llorca-Isern, S. Nicolopoulos, Orientation and phase mapping in the transmission electron microscope using precession-assisted diffraction spot recognition: state-of-the-art results, Journal of Microscopy. 252 (2013) 23–34. https://doi.org/10.1111/jmi.12065.

[48] E. Rauch, S. Rouvimov, S. Nicolopoulos, P. Moeck, High Throughput Automated Crystal Orientation and Phase Mapping of Nanoparticles from HREM - TEM Images, Microscopy and Microanalysis. 15 (2009) 756–757. https://doi.org/10.1017/S1431927609099607.

[49] M. Calcagnotto, D. Ponge, E. Demir, D. Raabe, Orientation gradients and geometrically necessary dislocations in ultrafine grained dual-phase steels studied by 2D and 3D EBSD, Materials Science and Engineering: A. 527 (2010) 2738–2746. https://doi.org/10.1016/j.msea.2010.01.004.

[50] Q. Liu, D. Juul Jensen, N. Hansen, Effect of grain orientation on deformation structure in cold-rolled polycrystalline aluminium, Acta Materialia. 46 (1998) 5819–5838. https://doi.org/10.1016/S1359-6454(98)00229-8.

[51] Y. Takayama, J.A. Szpunar, H. Kato, Analysis of Intragranular Misorientation Related to Deformation in an Al-Mg-Mn Alloy, Materials Science Forum. (2005). https://doi.org/10.4028/www.scientific.net/MSF.495-497.1049.

[52] A. Kumar, G. Agarwal, R. Petrov, S. Goto, J. Sietsma, M. Herbig, Microstructural evolution of white and brown etching layers in pearlitic rail steels, Acta Materialia. 171 (2019) 48–64. https://doi.org/10.1016/j.actamat.2019.04.012.

[53] M. Kawasaki, Z. Horita, T.G. Langdon, Microstructural evolution in high purity aluminum processed by ECAP, Materials Science and Engineering: A. 524 (2009) 143–150. https://doi.org/10.1016/j.msea.2009.06.032.

[54] Y. Ito, K. Edalati, Z. Horita, High-pressure torsion of aluminum with ultrahigh purity (99.9999%) and occurrence of inverse Hall-Petch relationship, Materials Science and Engineering: A. 679 (2017) 428–434. https://doi.org/10.1016/j.msea.2016.10.066.

[55] M.V. Markushev, E.V. Avtokratova, S.V. Krymskiy, O.Sh. Sitdikov, Effect of precipitates on nanostructuring and strengthening of high-strength aluminum alloys under high pressure torsion, Journal of Alloys and Compounds. 743 (2018) 773–779. https://doi.org/10.1016/j.jallcom.2018.02.047.

[56] R.K. Islamgaliev, N.F. Yunusova, I.N. Sabirov, A.V. Sergueeva, R.Z. Valiev, Deformation behavior of nanostructured aluminum alloy processed by severe plastic deformation, Materials Science and Engineering: A. 319–321 (2001) 877–881. https://doi.org/10.1016/S0921-5093(01)01052-8.

[57] R. Pippan, S. Scheriau, A. Taylor, M. Hafok, A. Hohenwarter, A. Bachmaier, Saturation of Fragmentation During Severe Plastic Deformation, Annual Review of Materials Research. 40 (2010) 319–343. https://doi.org/10.1146/annurev-matsci-070909-104445.

[58] Y. Huang, J.D. Robson, P.B. Prangnell, The formation of nanograin structures and accelerated room-temperature theta precipitation in a severely deformed Al–4wt.% Cu alloy, Acta Materialia. 58 (2010) 1643–1657. https://doi.org/10.1016/j.actamat.2009.11.008.

[59] X. Sauvage, F. Wetscher, P. Pareige, Mechanical alloying of Cu and Fe induced by severe plastic deformation of a Cu–Fe composite, Acta Materialia. 53 (2005) 2127–2135. https://doi.org/10.1016/j.actamat.2005.01.024.

[60] O. Cojocaru-Mirédin, D. Mangelinck, K. Hoummada, E. Cadel, D. Blavette, B. Deconihout, C. Perrin-Pellegrino, Snowplow effect and reactive diffusion in the Pt doped Ni–Si system, Scripta Materialia. 57 (2007) 373–376. https://doi.org/10.1016/j.scriptamat.2007.05.007.

[61] M.M. Abramova, N.A. Enikeev, R.Z. Valiev, A. Etienne, B. Radiguet, Y. Ivanisenko, X. Sauvage, Grain boundary segregation induced strengthening of an ultrafine-grained austenitic stainless steel, Materials Letters. C (2014) 349–352. https://doi.org/10.1016/j.matlet.2014.07.188.

[62] Y. Zhang, S. Jin, P.W. Trimby, X. Liao, M.Y. Murashkin, R.Z. Valiev, J. Liu, J.M. Cairney, S.P. Ringer, G. Sha, Dynamic precipitation, segregation and strengthening of an Al-Zn-Mg-Cu alloy (AA7075) processed by high-pressure torsion, Acta Materialia. 162 (2019) 19–32. https://doi.org/10.1016/j.actamat.2018.09.060.

[63] S.-S. Wang, J.-T. Jiang, G.-H. Fan, A.M. Panindre, G.S. Frankel, L. Zhen, Accelerated precipitation and growth of phases in an Al-Zn-Mg-Cu alloy processed by surface abrasion, Acta Materialia. 131 (2017) 233–245. https://doi.org/10.1016/j.actamat.2017.03.074.

[64] H. Zhao, F. De Geuser, A. Kwiatkowski da Silva, A. Szczepaniak, B. Gault, D. Ponge, D. Raabe, Segregation assisted grain boundary precipitation in a model Al-Zn-Mg-Cu alloy, Acta Materialia. 156 (2018) 318–329. https://doi.org/10.1016/j.actamat.2018.07.003.

[65] A. Deschamps, Y. Brechet, Influence of predeformation and ageing of an Al–Zn–Mg alloy—II. Modeling of precipitation kinetics and yield stress, Acta Materialia. 47 (1998) 293–305. https://doi.org/10.1016/S1359-6454(98)00296-1.

[66] C. Mangler, C. Gammer, H.P. Karnthaler, C. Rentenberger, Structural modifications during heating of bulk nanocrystalline FeAl produced by high-pressure torsion, Acta Materialia. 58 (2010) 5631–5638. https://doi.org/10.1016/j.actamat.2010.06.036.

[67] C. Gammer, H.P. Karnthaler, C. Rentenberger, Unexpected grain size reduction by heating in bulk nanocrystalline FeAl, Journal of Alloys and Compounds. 633 (2015) 384–389. https://doi.org/10.1016/j.jallcom.2015.01.186.

[68] E.V. Bobruk, M.Yu. Murashkin, V.U. Kazykhanov, R.Z. Valiev, Aging behavior and properties of ultrafine-grained aluminum alloys of Al-Mg-Si system, Reviews on Advanced Materials Science. 31 (2012) 109–115.

[69] I.F. Mohamed, S. Lee, K. Edalati, Z. Horita, S. Hirosawa, K. Matsuda, D. Terada, Aging Behavior of Al 6061 Alloy Processed by High-Pressure Torsion and Subsequent Aging, Metallurgical and Materials Transactions A: Physical Metallurgy and Materials Science. 46 (2015) 2664–2673. https://doi.org/10.1007/s11661-015-2840-5.

[70] K. Edalati, D. Akama, A. Nishio, S. Lee, Y. Yonenaga, J.M. Cubero-Sesin, Z. Horita, Influence of dislocation–solute atom interactions and stacking fault energy on grain size of single-phase alloys after severe plastic deformation using high-pressure torsion, Acta Materialia. 69 (2014) 68–77. https://doi.org/10.1016/j.actamat.2014.01.036.

[71] G. Sha, K. Tugcu, X.Z. Liao, P.W. Trimby, M.Y. Murashkin, R.Z. Valiev, S.P. Ringer, Strength, grain refinement and solute nanostructures of an Al–Mg–Si alloy (AA6060) processed by high-pressure torsion, Acta Materialia. 63 (2014) 169–179. https://doi.org/10.1016/j.actamat.2013.10.022.

[72] A. Mohammadi, N.A. Enikeev, M.Yu. Murashkin, M. Arita, K. Edalati, Examination of inverse Hall-Petch relation in nanostructured aluminum alloys by ultra-severe plastic deformation, Journal of Materials Science & Technology. 91 (2021) 78–89. https://doi.org/10.1016/j.jmst.2021.01.096.

Credit author statement :

Amandine Duchaussoy : Conceptualization, Investigation, Writing- Original draft preparation

Xavier Sauvage : Conceptualization, Writing - Review & Editing, Supervision

Alexis Deschamps : Conceptualization, Writing - Review & Editing, Supervision

Frederic De Geuser : Methodology, Software, Formal analysis , Writing - Review & Editing

Gilles Renou : Investigation, Review & Editing

Zenji Horita : Resources, Writing - Review & Editing

Declaration of interests

☒ The authors declare that they have no known competing financial interests or personal relationships that could have appeared to influence the work reported in this paper.

☐ The authors declare the following financial interests/personal relationships which may be considered as potential competing interests:

Highlights

Using HPS on a AlZnMgCu alloy leads to a microstructure close to the one obtained after HPT even a deformation 10 times lower.

The coexistence of GPzones and η’/η precipitates with approximatively the same evolutions during ageing for HPS and HPT processed samples are observed.

For both processes (HPS and HPT), an exceptional yield strength was obtained (>800MPa). After aging, a level only scarcely reached in aluminum alloys processed by SPD.